FISEVIER

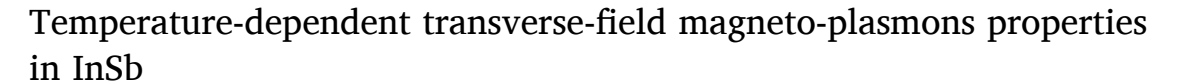
Contents lists available at ScienceDirect

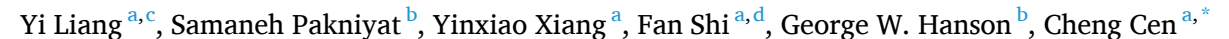
Optical Materials

journal homepage: http://www.elsevier.com/locate/optmat



Research Article





- a Department of Physics and Astronomy, West Virginia University, Morgantown, WV, 26506, USA
- ^b Department of Electrical Engineering, University of Wisconsin-Milwaukee, Milwaukee, WI, 53211, USA
- ^c Guangxi Key Lab for Relativistic Astrophysics, Center on Nanoenergy Research, School of Physical Science and Technology, Guangxi University, Nanning, Guangxi, 530004. China
- d Key Laboratory of Computer Vision and System of Ministry of Education, Tianjin University of Technology, Tianjin, 300384, China

ARTICLE INFO

Keywords: InSb Magneto-optical Plasmon Temperature Anisotropy

ABSTRACT

The coupling between plasmons and external fields can facilitate effective light manipulations. Here, we implement time-domain THz spectroscopy in a Voigt reflection geometry to study the transverse-field magneto-optical effects in indium antimonide (InSb) at variable temperatures. The obtained results are analyzed by a multi-carrier model, which allows the properties of both electrons and holes in undoped InSb to be fully characterized between 5 K and 300 K. At higher temperatures, the change in the thermal carrier density effectively modifies the dispersions of the three magneto-plasmon bands and produces strong reflectance modulations that can be sensitively tuned by the temperature. At low temperatures when the conduction is dominated by extrinsically doped electrons, a transport anisotropy in the (001) plane is detected. These results provide a systematic understanding on the magneto-plasmon band structure in InSb and their coupling with THz lights.

Narrow-gap semiconductors with high electron mobilities and low effective masses provide unique material platforms where carrier dynamics can effectively mediate the coupling between light and static fields [1]. One prototypical example is InSb [2–19], which hosts strong magneto-optical (MO) couplings that are tunable by temperature and doping [18–23]. In recent years, tailored MO effects in InSb have enabled a variety of intriguing functionalities, such as field induced transparency [12,22], nonreciprocal polarization rotation or optical isolation [18,19,24], and nontrivial photonic topology [11]. Besides these successful demonstrations, the interplay between the plasmonic charge oscillations and cyclotron resonances in InSb can also produce field-controlled reflectivity modulations with superior performances. Such effects produced at THz frequencies by intrinsic samples are less explored in the existing literature, and thus needs to be systematically mapped out, particularly at low temperatures.

In this work, we measure the THz reflectances of undoped InSb single crystals in a Voigt geometry with transverse magnetic fields up to 0.7 T and at varied temperatures from 5 K to 300 K. Due to the gapped bulk plasmon band structure, the measured reflectance is strongly modulated by the external field. The polarity, strength, and bandwidth of the modulation can all be flexibly tuned by controlling the plasma frequency

and the cyclotron frequency separately. The MO effect also sensitively traces the transport properties of electrons and holes in InSb, allowing the different conduction regions and a low-temperature anisotropy to be faithfully and contactlessly captured. These findings not only provide a clearer understanding on how the magnetic plasmon bands couple to the light reflections, but also yield important material parameters of InSb that are valuable for future active THz device developments.

Under a *y*-direction magnetic field B, the permittivity of a carrier plasma is [1,3,4,6,12,18,25]:

$$\mathbf{\varepsilon_r} = \begin{bmatrix} \varepsilon_t & 0 & i\varepsilon_g \\ 0 & \varepsilon_a & 0 \\ -i\varepsilon_g & 0 & \varepsilon_t \end{bmatrix} \tag{1}$$

For a semiconductor such as InSb, with one electron band and two hole bands near the Fermi level, the transverse (ε_t) , anomalous (ε_a) , and gyrotropic (ε_g) permittivity elements are: $\varepsilon_t = \varepsilon_\infty - \sum \frac{(\omega_p^{(j)})^2 (\omega + i \Gamma_j)}{\omega[(\omega + i \Gamma_j)^2 - (\omega_c^{(j)})^2]}$, where j = e, lh, hh indicates electron, light hole and heavy hole contributions, with corresponding effective mass m_i^* , density n_j , and mobility μ_i , ε_0 is the vacuum

E-mail addresses: pakniyat@uwm.edu (S. Pakniyat), cheng.cen@mail.wvu.edu (C. Cen).

^{*} Corresponding author.

Y. Liang et al. Optical Materials 112 (2021) 110831

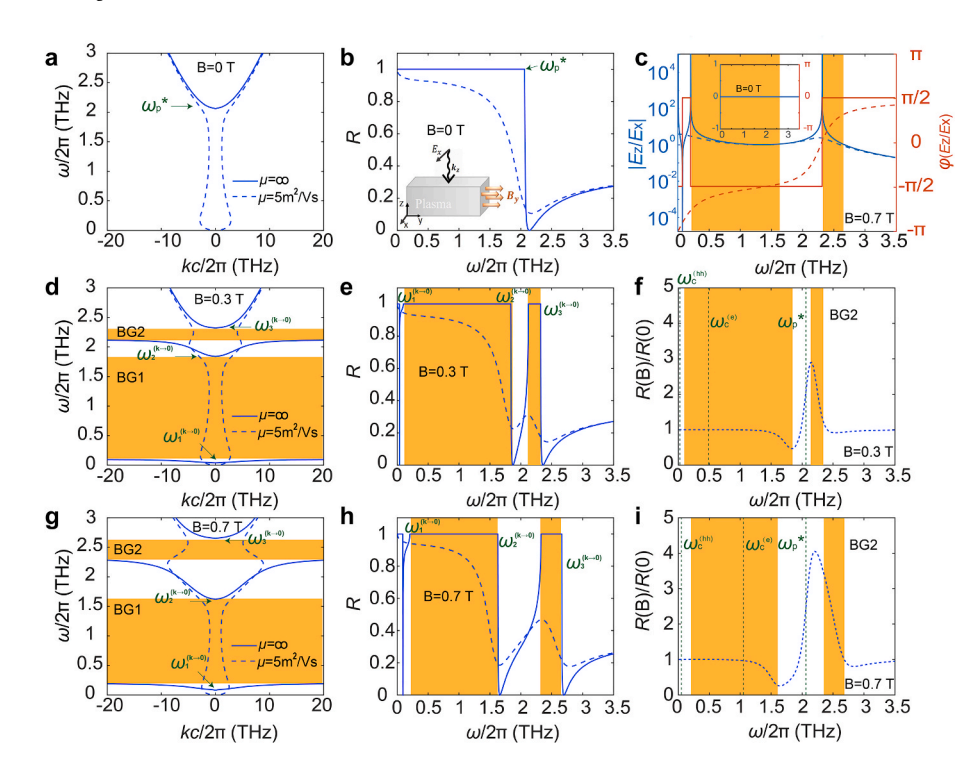


Fig. 1. Magnetic field induced bulk plasmon band gap (a, d, g) The calculated dispersion diagrams of TM bulk modes in isotropic (B = 0) and gyrotropic $(B \neq 0)$ plasma media. Room temperature carrier properties of an undoped InSb single crystal sample are used in this calculation: $n_e = 1.5 \times 10^{22} \, \text{m}^{-3}$, m_e * = $0.019m_0$, $n_{hh} = 1.49 \times 10^{22} \text{ m}^{-3}$, $m_{hh}^* = 0.43m_0$, $n_{lh} = 1.38 \times 10^{20} \text{ m}^{-3}, \, m_{lh}^* = 0.019 m_0, \, \varepsilon_{\infty} = 15.7.$ Blue solid curves correspond to the ideal dissipationless cases with $\mu_i = \infty$ and the dashed curves correspond to realistic cases with finite carrier mobilities of $\mu_e = \mu_{lh} = 5 \text{ m}^2 \text{ V}^{-1} \text{s}^{-1}$ and $\mu_{hh} = 0.01 \text{ m}^2 \text{ V}^{-1} \text{s}^{-1}$. (b, e, h) The calculated Voigt-configuration reflectance at an air/plasma interface. Inset in (b) shows the modeling and experiment geometry. (c) The polarization of TM mode at B = 0.7T and B = 0 T (inset). (f, i) The field-induced reflectance change calculated by dividing the nonzero-field reflectance by the zerofield value. In all plots, the two field-induced bandgaps are highlighted in grey.

permittivity, and ε_{∞} is the material permittivity at infinite frequency, $\omega_c^{(j)}=eB/m_j^*$ is the cyclotron frequency, $\Gamma_j=e/\mu_j m_j^*$ is the carrier scattering rate, $\omega_p^{(j)}=\sqrt{n_j e^2/m_j^* \varepsilon_0}$ is the plasma frequency.

The effective masses of the different carriers in InSb vary as $m_e^* \approx$

 $m_{lh}^* \ll m_{hh}^*$. Since the density of impurities in undoped single crystals is low, the samples studied in this work are quasi-intrinsic semiconductors where $n_e \approx n_{hh} + n_{lh}$. Under these conditions, the characteristic frequencies associated with the three carrier species follow the relations of $\omega_p^{(e)} \gg \omega_p^{(hh)} > \omega_p^{(h)}$ and $\omega_c^{(e)} \approx \omega_c^{(lh)} \gg \omega_c^{(hh)}$. As a result, the THz responses of

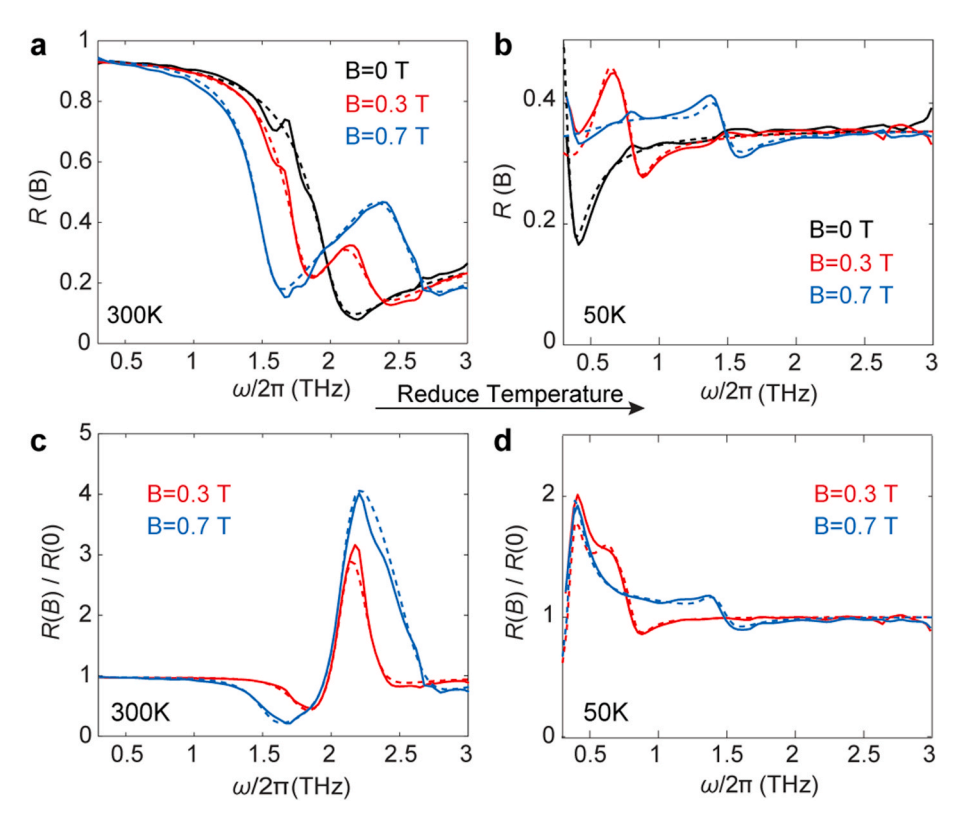


Fig. 2. Field-dependent THz reflectances of undoped InSb (a, b) Reflectance spectra of InSb at 300K and 50K measured under different in-plane magnetic fields. (c, d) Corresponding field-induced reflectance changes comparing data obtained with and without a magnetic field. Dashed curves in (a-d) show the fitting results based on Eq. (3).

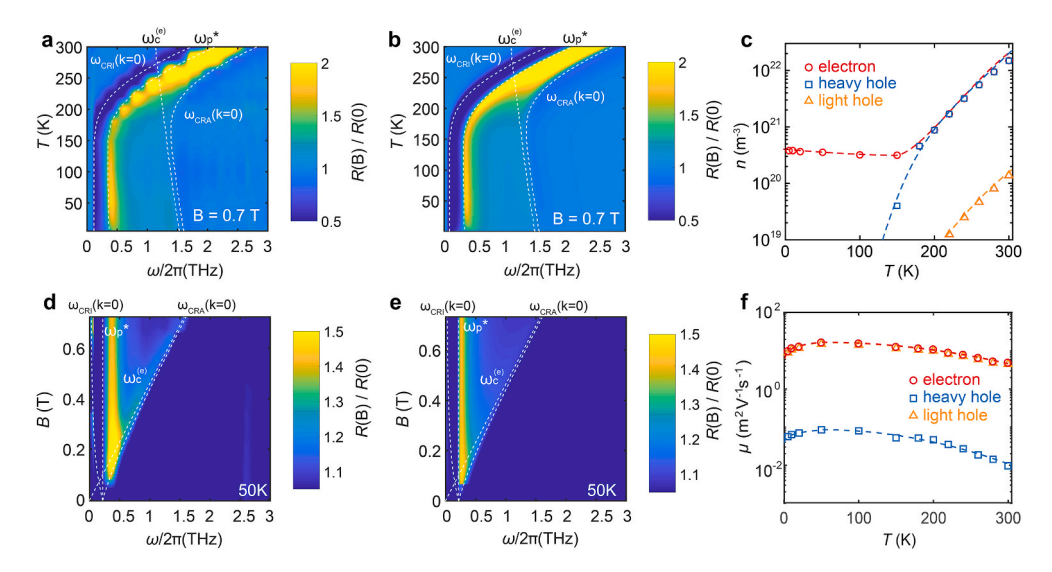


Fig. 3. Temperature dependences of the magneto-plasmonic properties (a, b, d, e) Temperature-frequency (a, b) and magnetic field-frequency (d, e) diagrams of the THz reflectance. Dashed lines trace the changes in the critical frequencies. (a, d) show the experimental data, and (b, e) show the simulated results. (c, f) Temperature-dependent changes in the carrier densities(c), mobilities(f) of electron, heavy hole, light hole.

the samples are mainly determined by electrons, though at frequencies near $\omega_c^{(hh)}$ the effects of heavy hole cyclotron resonance is also significant.

Plane waves propagating in such a gyrotropic medium are superpositions of TE modes (electric field polarizes along the magnetic field orientation) and TM modes (electric field polarizes perpendicular to the magnetic field). In this work, we focus on the TM modes, which follow the dispersion relation of [1,3,4,6,12,18,25]:

$$k_{TM}^2 = \varepsilon_{eff} k_0^2 = \frac{\varepsilon_t^2 - \varepsilon_g^2}{\varepsilon_t} \frac{\omega^2}{c^2}$$
 (2)

The polarizations of the TM modes are determined by: $E_z/E_x = -i\varepsilon_g/\varepsilon_t$. At zero field (B=0), TM modes are linearly polarized (Fig. 1c, inset) and only present above the normalized plasma frequency $\omega_p^* =$

 $\sqrt{\sum (\omega_p^{(j)})^2/\varepsilon_\infty}$ (Fig. 1a). When a nonzero magnetic field is applied, this single bulk optical band splits into three (Fig. 1d, g). The lowest band, unique in the multi-carrier case, is produced by the field responses of the electron-hole hybrid [1]; The middle band is right-elliptically polarized (Fig. 1c) and called the cyclotron resonance in-active (CRI) mode [1]. The highest band, left-elliptically polarized, is called the cyclotron resonance active (CRA) mode. The three bands are separated by two bandgaps: BG1 and BG2. As shown in Fig. 1d and g, the positions and sizes of the bandgaps are field-dependent. In the large field limit ($B \rightarrow \infty$), BG1 closes near the heavy hole cyclotron frequency $\omega_c^{(hh)}$, and the bottom edge of BG2 asymptotically approaches the electron cyclotron frequency $\omega_c^{(e)}$.

The presence of field-induced bulk optical bandgaps strongly modulates the reflectance of light incidences that follow the Voigt configuration (inset in Fig. 1b). Solving the wave equation while considering the continuity of tangential components of the electric and magnetic fields at the boundary, we obtain the reflection coefficient for a TM plane wave that incidents normally from a semi-infinite dielectric medium (with an isotropic permittivity ε_d) to a semi-infinite gyrotropic plasma,

$$r_{TM} = \frac{\sqrt{\varepsilon_{eff}} - \sqrt{\varepsilon_d}}{\sqrt{\varepsilon_{eff}} + \sqrt{\varepsilon_d}}$$
 (3)

Fig. 1b, e and h plot the reflectance $(R = |r_{TM}|^2)$ spectra for an air/plasma interface $(\varepsilon_d = 1)$ under different field strengths. Near-unity reflectances are found inside BG1 and BG2, whereas the reflectances in each TM band are significantly suppressed.

In realistic materials with finite carriers mobilities, the nonzero carrier scattering rates lead to modified plasmon dispersions (dashed curves, Fig. 1a, d, g). True energy gaps that strictly forbid the bulk plasmon propagation no longer exist, but the optical densities of states inside the bandgaps remain low. Correspondingly, although the reflectance spectra (dashed curves, Fig. 1b, e, h) deviate from the ideal lossless cases, the magneto-optic modulations near the plasmon bandgap are still very significant. Fig. 1f and i highlight the field effects by calculating the ratio between the nonzero-field reflectance (R(B)) and the zero-field reflectance (R(0)). The field-induced reflectance modulation is particularly strong in the frequency window covering the CRI band and BG2. As already discussed, the bandwidth of such frequency window increases with the external field.

To study the field-controlled reflectance changes in experiments, we perform terahertz time-domain spectroscopy (THz-TDS) measurements in Voigt configuration on nominally undoped (001) InSb single crystals (MTI Corp.) at different temperatures and fields. Fig. 2a and b show the variable-field reflectance spectra obtained at 300 K and 50 K. Here, the absolute reflectance R(B) is measured using an Au plate as the reference, which has near-constant THz reflectances below 3 THz (More experimental detail can be find in Supplemental Material). Due to the positioning error associated with the sample exchange and the atmospheric light absorptions [12] that varies as the lab humidity fluctuates, minor spurious signals in R(B) are inevitable. In comparison, the self-referenced field-induced reflectance change spectra R(B)/R(0) tends to be more robust (Fig. 2c and d). At 300 K, a single reflectance enhancement peak near 2.2 THz is detected (Fig. 2c). As shown by the theoretical calculation (Fig. 1f, i), the position of this peak is field-independent and determined by ω_p^* . At 50 K, this peak moves to 0.45 THz, indicating a much lower plasma frequency caused by the weakened thermal activation of carriers. Since ω_p^* is very low at 50 K, BG2 becomes well separated from ω_p^* even for small magnetic fields. As a result, a second peak emerges in R(B)/R(0), which has a field-dependent center frequency that traces the position of BG2 ($\sim \omega_c^{(e)}$) (Fig. 2d). For both temperatures, the observed data can be well fitted by the theoretical model as described by Eq. (3) (dashed line curves, Fig. 2a-d).

To better visualize the dependences of the light reflection on temperature and field, we plot the experimental data obtained at 5 K \leq $T \leq$ 300 K and 0 T \leq $B \leq$ 0.7 T in forms of temperature-frequency and field-frequency diagrams (Fig. 3a, d). For comparison, theoretical calculation results are also shown in Fig. 3b and e. On these diagrams,

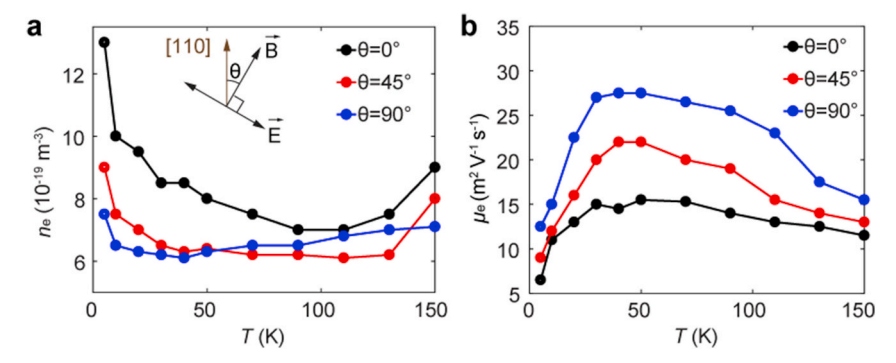


Fig. 4. Anisotropy of carrier properties in InSb. (a, b) Temperature-dependent electron density (a) and mobility (b) measured at different in-plane sample rotations. As shown by the inset of (a), θ marks the angle between the external magnetic field and the [110] lattice axis.

the changes in critical frequencies, including $\omega_c^{(e)}$, ω_p^* , and the lower edges of CRI, CRA bands ($\omega_{CRI}(k=0)$, $\omega_{CRA}(k=0)$) are traced by dashed lines

Clearly, the field-induced reflectance modulations mainly occur within the frequency range between $\omega_{CRI}(k=0)$ and $\omega_{CRA}(k=0)$. Such frequency window is wider at low temperatures when ω_p^* is much smaller than $\omega_c^{(e)}$. The width reaches 1.2 THz at 50 K for a field of 0.7 T. The reflectance is enhanced by the magnetic field for frequencies above ω_p^* , and suppressed for frequencies below ω_p^* . As the temperature drops from 300K to 150 K, since ω_p^* is reduced by more than 80%, the polarity of field-induced reflectance change alters for a wide range of light frequencies. In comparison, $\omega_c^{(e)}$ only depends on the temperature weakly due to the small reduction in effective mass [26]. At a fixed temperature, R(B)/R(0) is largest when ω_p^* and $\omega_c^{(e)}$ are in resonance.

Based on the THz reflectance data, temperature-dependent carrier parameters in the undoped InSb sample are extracted (Fig. 3c, f). Above 150 K, the conduction in InSb is dominated by thermally activated intrinsic carriers. Consequently, the change in electron and hole densities follows the Arrhenius law $(n \sim \exp\left(-\frac{E_a}{2kT}\right))$, where the activation energy $E_a \sim 0.29$ eV represent the electronic bandgap size. Below 150 K, as the population of the thermally excited intrinsic carriers diminishes, extrinsic carriers doped from ionized impurities prevail, leading to the nearly constant $10^{2\bar{0}}\,\mathrm{m}^{-3}$ level low-temperature electron densities. The changes in electron and holes mobilities also fall into two temperature regimes (Fig. 3f). At higher temperatures (T > 50 K), electron-phonon interaction is the dominant venue of carrier scattering in InSb [23]. As the phonon density decreases with the reducing temperature, carrier mobilities rise. This trend is however reversed for temperatures below 50 K. Such behavior is due to the scattering between carriers and the charged impurity dopants, which dominates over the carrier-phonon scattering process at low temperatures and is stronger when the thermal energy is low.

By rotating the sample in-plane, carrier properties along different directions in the (001) plane can be characterized and compared. While the THz magneto-reflectance is largely isotropic at room temperature, clear anisotropy is observed at low temperatures. As shown in Fig. 4, the low temperature carrier mobility is highest along the [110] crystal axis, and lowest along the [1 $\overline{10}$] axis (Fig. 4b). The trend of the electron density is opposite to the mobility, which minimizes along the [110] axis and maximizes along the [1 $\overline{10}$] axis (Fig. 4a). Such uniaxial anisotropy, distinct from the Hamiltonian calculated based on the Zincblende cubic lattice structure [27], is likely caused by the anisotropic energy profile associated with the impurity dopants. Consistent with this attribution, similar anisotropy was not observed in experiments where the effects related to the impurity doping are weak, such as when high-purity samples are used [28] or when intrinsic thermal carriers dominate [10].

In summary, we have modeled and characterized the THz reflectance

of undoped InSb single crystals for a wide range of temperatures and fields. Out of the three bulk TM bands, the field-induced reflectance modulations mainly come from the two electron dominated ones (CRI and CRA), whereas the contribution from the electron-hole hybrid band is very weak. By tuning the plasma frequency and cyclotron frequency relative to each other, the overall profile of the magneto-reflectance spectrum can be flexibly modified, allowing control over both the strength and the polarity of the field effect. Additionally, contactless measurements of the temperature-dependent carrier parameters in InSb are also obtained from 5K to 300K, yielding results highly useful for future device design.

Data availability

The data that support the findings of this study are available from the corresponding author upon request.

Supplementary information

Additional plots and discussions on the reflectance equation derivation and low temperature bulk band structure are available in the supplementary information.

CRediT authorship contribution statement

Yi Liang: Investigation, Writing - original draft, Software, Visualization, Formal analysis. Samaneh Pakniyat: Methodology, Software, Visualization, Formal analysis. Yinxiao Xiang: Software, Methodology, Formal analysis. Fan Shi: Investigation. George W. Hanson: Conceptualization, Methodology, Software, Data curation, Validation. Cheng Cen: Conceptualization, Writing - review & editing, Resources, Visualization, Supervision, Project administration.

Declaration of competing interest

The authors declare that they have no known competing financial interests or personal relationships that could have appeared to influence the work reported in this paper.

Acknowledgements

The authors would like to acknowledge the support of the US NSF grant No.1741673, the National Natural Science Foundation of China (11604058, 11704081), and the Guangxi Natural Science Foundation (No. 2016GXNSFBA380244).

Appendix A. Supplementary data

Supplementary data to this article can be found online at https://doi.org/10.1016/j.optmat.2021.110831.

References

- [1] E.D. Palik, J.K. Furdyna, Infrared and microwave magnetoplasma effects in semiconductors, Rep. Prog. Phys. 33 (1970) 1193.
- [2] B.H. Cheng, H.W. Chen, K.J. Chang, Y.C. Lan, D.P. Tsai, Magnetically controlled planar hyperbolic metamaterials for subwavelength resolution, Sci. Rep. 5 (2015) 18172.
- [3] B. Hu, Y. Zhang, Q.J. Wang, Surface magneto plasmons and their applications in the infrared frequencies, Nanophotonics 4 (2015) 383–396.
- [4] J. Chochol, K. Postava, M. Čada, M. Vanwolleghem, L. Halagačka, J.-F. Lampin, J. Pištora, Magneto-optical properties of InSb for terahertz applications, AIP Adv. 6 (2016) 115021.
- [5] P. Kumar, M. Kumar, V.K. Tripathi, Linear mode conversion of terahertz radiation into terahertz surface magnetoplasmons on a rippled surface of magnetized n-InSb, Optic Lett. 41 (2016) 1408–1411.
- [6] F. Fan, S. Chen, S.-J. Chang, A review of magneto-optical microstructure devices at terahertz frequencies, IEEE J. Sel. Top. Quant. Electron. 23 (2017) 1–11.
- [7] S. Lin, K. Bhattarai, J. Zhou, D. Talbayev, Giant THz surface plasmon polariton induced by high-index dielectric metasurface, Sci. Rep. 7 (2017) 9876.
- [8] S. Yu, K.H. Heffernan, D. Talbayev, Beyond the effective mass approximation: a predictive theory of the nonlinear optical response of conduction electrons, Phys. Rev. B 95 (2017).
- [9] D. Yavorskiy, K. Karpierz, M. Grynberg, W. Knap, J. Łusakowski, Indium antimonide detector for spectral characterization of terahertz sources, J. Appl. Phys. 123 (2018), 064502.
- [10] S. Houver, L. Huber, M. Savoini, E. Abreu, S.L. Johnson, 2D THz spectroscopic investigation of ballistic conduction-band electron dynamics in InSb, Optic Express 27 (2019) 10854–10865.
- [11] D. Wang, B. Yang, W. Gao, H. Jia, Q. Yang, X. Chen, M. Wei, C. Liu, M. Navarro-Cía, J. Han, W. Zhang, S. Zhang, Photonic Weyl points due to broken time-reversal symmetry in magnetized semiconductor, Nat. Phys. 15 (2019) 1150–1155.
- [12] F. Li, F. Fan, Y. Ji, Z. Tan, Q. Mu, S. Chang, Terahertz tunable filter and modulator based on magneto plasmon in transverse magnetized InSb, Optic Lett. 45 (2020) 1–4.
- [13] Z.-Y. Tan, F. Fan, S.-J. Chang, Active broadband manipulation of terahertz photonic spin based on gyrotropic Pancharatnam-Berry metasurface, IEEE J. Sel. Top. Quant. Electron. (2020) 1, 1.
- [14] S.M. Hanham, A.I. Fernandez-Dominguez, J.H. Teng, S.S. Ang, K.P. Lim, S.F. Yoon, C.Y. Ngo, N. Klein, J.B. Pendry, S.A. Maier, Broadband terahertz plasmonic response of touching InSb disks, Adv. Mater. 24 (2012) OP226–230.

- [15] B. Hu, Q.J. Wang, Y. Zhang, Slowing down terahertz waves with tunable group velocities in a broad frequency range by surface magneto plasmons, Optic Express 20 (2012) 10071–10076.
- [16] B. Hu, Q.J. Wang, Y. Zhang, Broadly tunable one-way terahertz plasmonic waveguide based on nonreciprocal surface magneto plasmons, Optic Lett. 37 (2012) 1895–1897.
- [17] L. Deng, J. Teng, H. Liu, Q.Y. Wu, J. Tang, X. Zhang, S.A. Maier, K.P. Lim, C.Y. Ngo, S.F. Yoon, S.J. Chua, Direct optical tuning of the terahertz plasmonic response of InSb subwavelength gratings, Adv. Opt. Mater. 1 (2013) 128–132.
- [18] S. Lin, S. Silva, J. Zhou, D. Talbayev, A one-way mirror: high-performance terahertz optical isolator based on magnetoplasmonics, Adv. Opt. Mater. 6 (2018) 1800572
- [19] Q. Mu, F. Fan, S. Chen, S. Xu, C. Xiong, X. Zhang, X. Wang, S. Chang, Tunable magneto-optical polarization device for terahertz waves based on InSb and its plasmonic structure, Photon. Res. 7 (2019) 325.
- [20] M. Oszwalldowski, M. Zimpel, Temperature dependence of intrinsic carrier concentration and density of states effective mass of heavy holes in InSb, J. Phys. Chem. Solid. 49 (1988) 1179–1185.
- [21] S.C. Howells, L.A. Schlie, Transient terahertz reflection spectroscopy of undoped InSb from 0.1 to 1.1 THz, Appl. Phys. Lett. 69 (1996) 550–552.
- [22] X. Wang, A.A. Belyanin, S.A. Crooker, D.M. Mittleman, J. Kono, Interferenceinduced terahertz transparency in a semiconductor magneto-plasma, Nat. Phys. 6 (2009) 126–130.
- [23] K. Alfaramawi, M.A. Alzamil, Temperature-dependent scattering processes of ntype indium antimonide, Optoelectron. Adv. Mater. Rapid Commun. 3 (2009) 569–573
- [24] F. Fan, S.-T. Xu, X.-H. Wang, S.-J. Chang, Terahertz polarization converter and one-way transmission based on double-layer magneto-plasmonics of magnetized InSb, Optic Express 24 (2016) 26431–26443.
- [25] G.E. Smith, L.C. Hebel, S.J. Buchsbaum, Hybrid resonance and "Tilted-Orbit" cyclotron resonance in bismuth, Phys. Rev. 129 (1963) 154–168.
- [26] G. Carelli, N. Ioli, A. Messina, A. Moretti, S. Schepis, F. Strumia, Temperature dependence of InSb reflectivity in the far infrared: determination of the electron effective mass, Int. J. Infrared Millimet. Waves 19 (1998) 1191–1199.
- [27] M.H. Weiler, R.L. Aggarwal, B. Lax, Warping- and inversion-asymmetry-induced cyclotron-harmonic transitions in InSb, Phys. Rev. B 17 (1978) 3269–3283.
- [28] W. Zawadzki, I.T. Yoon, C.L. Littler, X.N. Song, P. Pfeffer, Anisotropy of the conduction band of InSb: orbital and spin properties, Phys. Rev. B 46 (1992) 9469–9475.